https://doi.org/10.20965/jdr.2017.p0259

Paper:

Object-Based Building Damage Assessment Methodology Using Only Post Event ALOS-2/PALSAR-2 Dual Polarimetric SAR Intensity Images

Yanbing Bai[*,†], **Bruno Adriano**[**], **Erick Mas**[**], **Hideomi Gokon**[***], **and Shunichi Koshimura**[**]

[*]Graduate School of Engineering, Tohoku University
Aoba 468-1, Aramaki, Aoba-ku, Sendai 980-0845, Japan
[†]Corresponding author, E-mail: bai.yanbing.q3@dc.tohoku.ac.jp
[**]International Research Institute of Disaster Science, Tohoku University, Sendai, Japan
[***]Institute of Industrial Science, The University of Tokyo, Tokyo, Japan
[Received October 4, 2016; accepted February 4, 2017]

Earthquake-induced building damage assessment is an indispensable prerequisite for disaster impact assessment, and the increasing availability of high-resolution Synthetic Aperture Radar (SAR) imagery has made it possible to construct damaged building inventories soon after earthquakes strike. However, the shortage of pre-seismic SAR datasets and the lack of available building footprint data pose challenges for rapid building damage assessment. Taking advantage of recent advances in machine learning algorithms, this study proposes an object-based building damage assessment methodology that uses only post-event SAR imagery. A Random Forest machine learning-based object classification, a simplified approach to the extraction of built-up areas, was developed and tested on two ALOS2/PALSAR-2 dual polarimetric SAR images acquired in affected areas soon after the 2015 Nepal earthquake. In addition, a series of texture metrics as well as the random scattering metric and reflection symmetry metric were found to significantly enhance classification accuracy. The feature selection was found to have a positive effect on overall performance. Moreover, the proposed Random Forest framework resulted in overall accuracies of 93% with a kappa coefficient of 0.885 when the object scale of 60 × 60 pixels and 15 features were adopted. A comparative experiment with the k-nearest neighbor framework demonstrated that the Random Forest framework is a significant step toward the achievement of a balanced, two-class classification.

Keywords: 2015 Nepal earthquake, object-based building damage assessment, post-event dual-polarimetric SAR imagery, Random Forest machine learning algorithms

1. Introduction

Natural disasters, especially earthquakes, are rapid and extreme events that result in significant losses of life and damage to property. During the period 2001∼2011, disasters caused more than 780,000 deaths and earthquakes accounted for nearl 60% of all disaster-related casualties [1]. More than a million earthquakes occur worldwide every year, approximately two earthquakes per minute. Rapid and effective earthquake disaster estimation enables governments to make better responses to disasters. However, such rapid estimation is still a challenge faced by governments and experts alike [2]. The estimation of earthquake-induced building damage was initially achieved by integrating the manual visual interpretation of high-resolution satellite images and field work [3, 4]. Despite its relatively high accuracy, the applicability of this technique is highly restricted by its time-consuming nature. To mitigate the disadvantages of manual interpretation, a series of quick, automatic building-damage estimation approaches from multitemporal optical images [5, 6] and SAR image [7–9] have been proposed. However, as these methodologies are based on change detection techniques using multitemporal images, cloud cover effects and the lack of suitable pre-event archives pose immense challenges for any multitemporal image-based mapping approach or optical remote sensing technique. This fact has been highlighted by large events such as the 2015 Gorkha earthquake in Nepal, the 2009 LÁquila earthquake in Italy, and the 2008 Wenchuan earthquake and 2010 Yushu earthquake in China.

Under the circumstances, the exploitation of building damage assessment using only post-event SAR remote-sensing images has garnered broad attention and has already demonstrated its preliminary potential for building damage assessment [10–12]. The approaches that have been proposed can be generally classified into pixel-based and object-based techniques, and they often make use of ancillary datasets such as building footprint data. Since the pixel-based techniques [12] mainly rely on the backscattering coefficient signal of individual pixels, the results are easily affected by speckle effects. To address such issues, a novel strategy, object-based analysis, has come to be used for building damage classification. However, critical challenges still exist when only a single, carefully-selected feature is used for classifica-

Table 1. Characteristics of ALOS-2/PALSAR-2 images used for this study.

Date	Polarization	Spatial Resolution	Off-nadir angle	Pass	Range direction	Level
2015/05/02	HH+HV	10m(Fine)	32.5°	Ascending	Right	SLC
2015/04/26	HH+HV	3m(Ultrafine)	44.7°	Ascending	Right	GRD

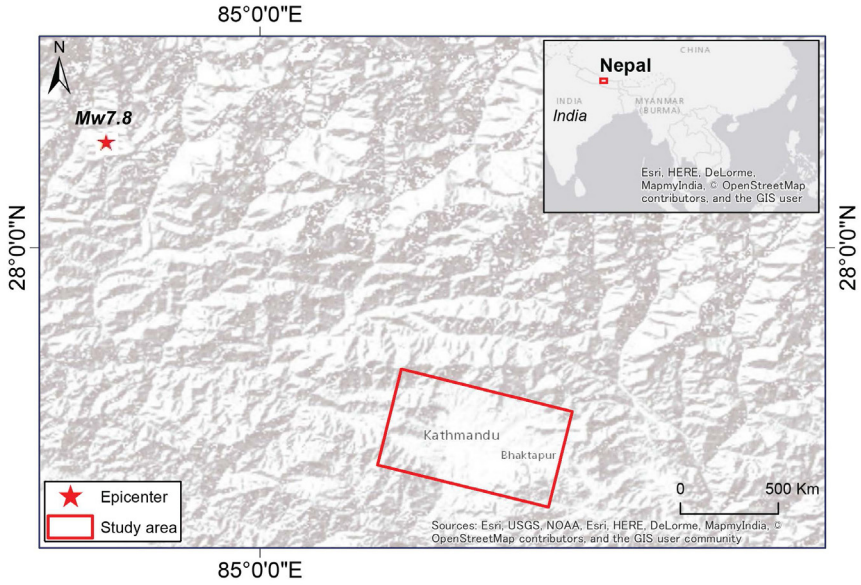

Fig. 1. Location of study area in Kathmandu, Nepal.

tion [12, 13]. In addition, the great variety of types of building damage and the available types of remote sensing imagery (imagery acquisition conditions and polarization types) largely limit the transferability of the proposed methods and the development of operational workflows.

Recently, a machine learning algorithm which utilizes high-dimensional features has played an important role in the remote sensing field [14]. The machine learning algorithms in particular, such as Random Forest (RF) [15], have demonstrated excellent performance in the analyses of many complex, remote sensing datasets [16–18]. Machine learning algorithms have also been successfully applied to land cover mapping [19] and volcanic deposits mapping [20] using SAR imagery. However, limited research has been carried out on earthquake-induced building damage mapping in this field, so little is known about the robustness or applicability of building damage mapping using machine learning algorithms and object-based mapping techniques. Thus, the objective of this study was to develop a building-damage assessment methodology using only post-event SAR imagery by integrating the RF machine learning algorithm and object-based analysis techniques.

2. Study Area and Datasets

The area studied in this research is located in the Kathmandu valley, including the towns of Sankhu and Bhaktapur, as shown in **Fig. 1**. This was one of the most devastated areas in the 2015 Nepal earthquake. In this event, 67,871 fully-damaged buildings and 73,624 partially-damaged buildings were reported in the Kathmandu valley [21].

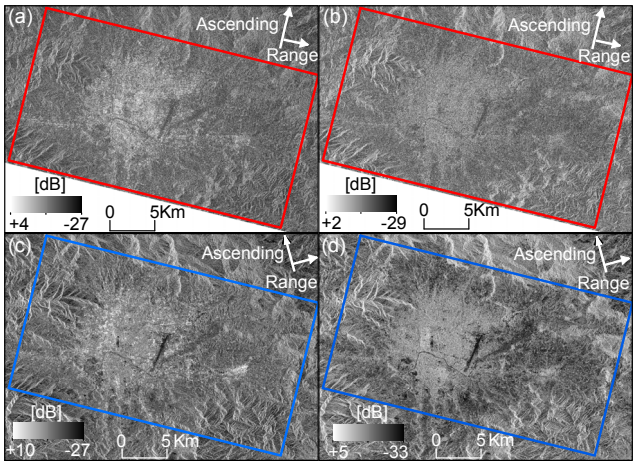

Fig. 2. ALOS-2/PALSAR-2 data used in this study. (a) and (b) are the HH and HV backscattering coefficient image calculated from ALOS-2/PALSAR-2 image acquired on April 26, 2015. (c) and (d) are the HH and HV backscattering coefficient image calculated from the ALOS-2/PALSAR-2 image acquired on May 2, 2015.

The data used in this study includes two L-band ALOS-2/PALSAR-2 dual-polarization (HH/HV) datasets, the details of which are summarized in **Table 1**. The GRD [22] dataset, acquired on April 26, 2015 with a spatial resolution of 3 m, was used as the main data source of this

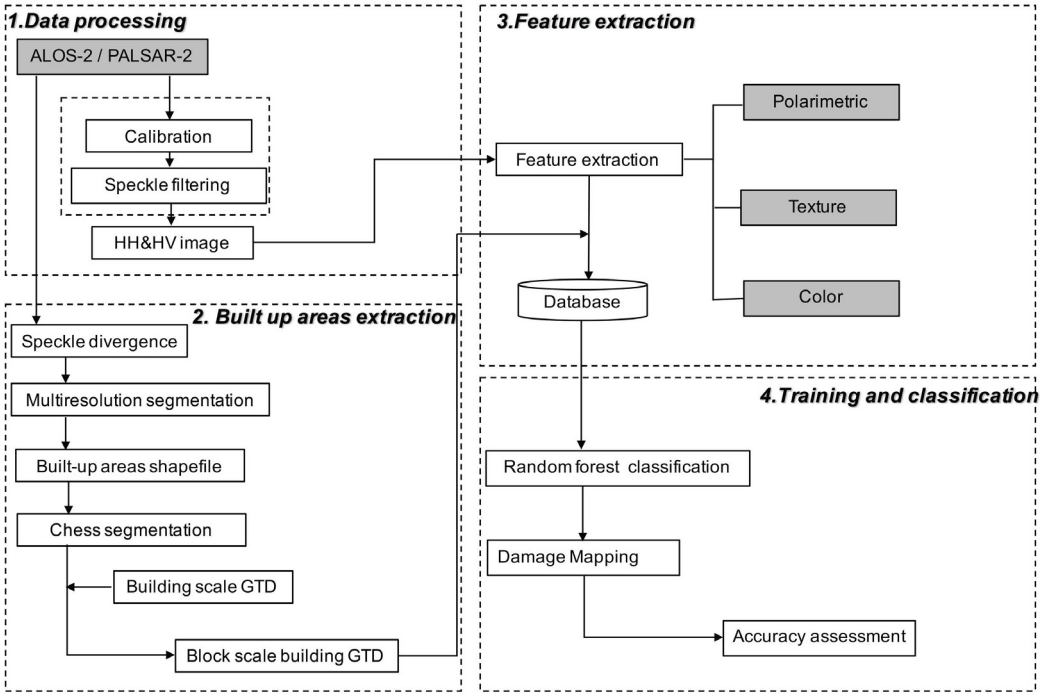

Fig. 3. Flowchart summarizing the processing steps for building damage mapping.

research because of its high resolution. However, as the GRD data are represented by amplitude data and do not contain the phase information that can be used for polarimetric information extraction, another Single Look Complex (SLC) dataset, acquired on May 2, 2015 with a 10 m-resolution, was employed as a substitute.

First, the SLC data were multi-looked (6 looks in azimuth and 3 looks in range) and geocoded using ENVI/SARscape 5.2 software. Together with the GRD dataset, radiometric calibration was performed to get a backscattering coefficient in decibel (dB) units. Then, the enhanced Lee filter (3 $\times$ 3) was applied to reduce the speckle effect. All the images for the co-polarization (HH) and cross-polarization (HV) data are shown in **Figs. 2(a, b, c, d)**.

3. Methodology

First, a simplified speckle divergence-based methodology was proposed to extract the built-up area (BA), and then the BA shape was split up into multi-scale size to generate the object ground truth data (GTD). Then, a comprehensive set of metrics, including 15 polarimetric, 83 texture, and 4 color metrics, was calculated.The metrics were integrated with the object ground truth data to construct the database for classification. Finally, a Random Forest (RF) machine learning approach was introduced, and bootstrap-sampling-based out of bag (OOB) testing was used for the accuracy evaluation and grading of the variable importance score. The steps of the process are shown in detail in **Fig. 3**.

3.1. Simplified Object-Based BA Extraction

In this paper, the methodology for BA extraction was developed based on the method proposed by [23]. In accordance with [23], ten thresholds were used to extract the BA, although this greatly increases the complexity of building extraction and is not conducive to real disaster emergency responses. However, we aimed at developing a simplified technique for quick BA extraction based on one single-polarized ALOS-2/PALSAR-2 SAR intensity image. The procedure consists of two main steps: 1) the speckle divergence image calculation, and 2) the object-based mapping of BA.

3.1.1. Speckle Divergence Calculation

In this paper, the ultrafine stripmap SAR intensity data shown in **Fig. 4(a)** were employed to generate the speckle divergence image. In order to determine the best window size for the calculation of the speckle divergence image, the building sizes in Kathmandu were analyzed based on the available building footprint data (125,314 buildings), and the results showed that most of the buildings were within 225 m^2. Ideally,this size is equal to 5 $\times$ 5 pixels window size in the corresponding SAR image, but the actual window size should be larger than 5 $\times$ 5 pixels due to the complexity of the building shapes. Finally, the 9 $\times$ 9-pixel window size was adopted as the optimal window size used in calculating the speckle divergence image, as shown in **Fig. 4(b)**. This is because using a window size smaller than 7 $\times$ 7 pixels cannot guarantee that most kinds of buildings can be completely represented in such a small patch image. Using a window size larger than 11 $\times$ 11 pixels would decrease the precision of spatial localization [23].

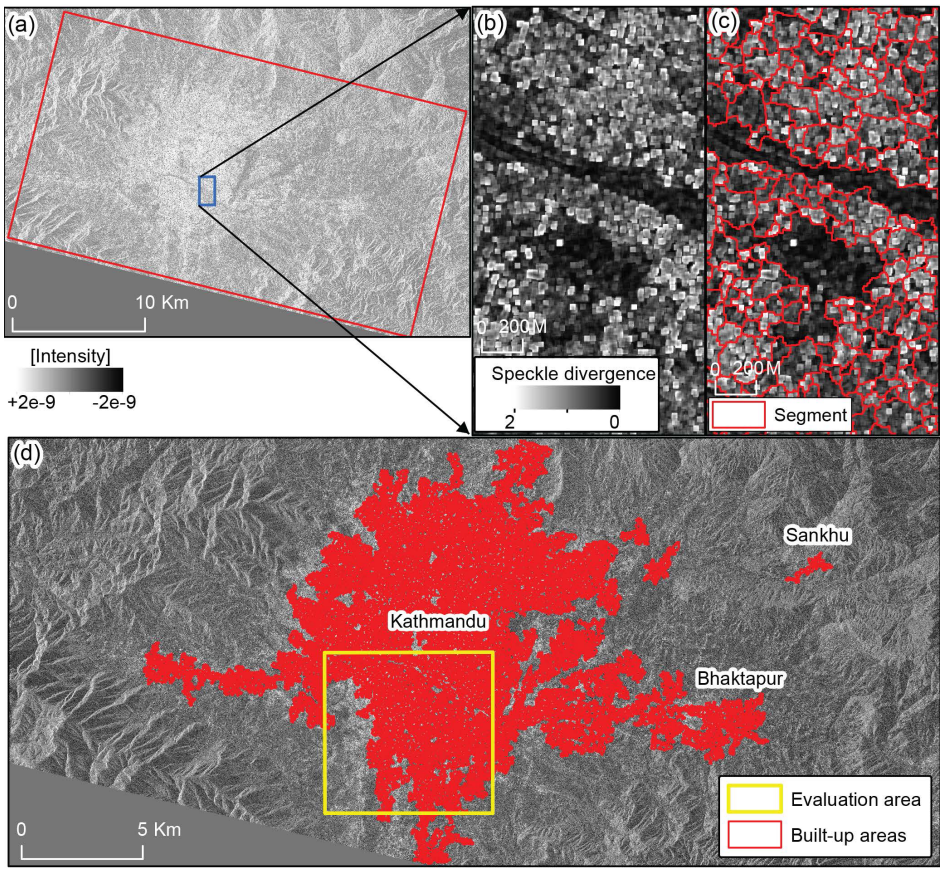

Fig. 4. Result of built-up area extraction. (a) The original SAR intensity image. (b) Speckle divergence image (c) Result of multiresoultion segmentation. (d) Extracted built-up areas. The yellow rectangle is the area used for accuracy assessment of extracted built-up areas.

3.1.2. Object-Based BA Extraction

The first step in BA extraction is image segmentation, for which we used the multiresolution segmentation algorithm provided by eCognition software. The segmentation was performed using the speckle divergence image that originated from the ultrafine stripmap copolarization SAR intensity image (26 April 2015,07:01:53 UTC). A series of segments were generated as shown in **Fig. 4(c)**. The parameter settings for segmentation are as follows: scale parameter, 10 × 10 pixels; shape, 0.1; color, 0.9; smoothness, 0.5; and compactness, 0.5. Based on the image segmentation, the next goal is to develop a simple rule base for extracting the BA areas. Assuming that all BAs include segments with high brightness, the key point is to determine the best threshold value (T), based on the brightness value of the speckle divergence image within the segments used for the extraction of the BA. Several threshold values from 0.1 to 0.7 were tested. The detected BAs were visually compared with the BA in the optical image, and the threshold $T = 0.5$ was selected for the extraction of the candidate BA because it showed the best performance. Next, a region merge algorithm was employed to merge all the above extracted segments to produce bigger segments, and then all the small, isolated segments were removed. The final BA can be seen in **Fig. 4(d)**.

3.2. Generation of Block Object Ground Truth Data

Regarding the building damage classification using only post-event SAR imagery, the basic idea is to identify the differences between damaged buildings and undamaged buildings, based on the radar scattering characteristics in the same single-phase image. This is quite different from the principle of change-detection-based building damage assessment. It is very important to carry out the building damage classification on the block scale by grasping the overall characteristics of the affected buildings instead of on the single building scale within its building footprint area. The reasons are as follows. 1) Due to the variety of types of earthquake-induced damage to buildings, the backscattering coefficient values will be different not only within the building footprint outline but also in the neighboring pixels. 2) Due to the side-looking effect of radar observation, the shadow areas and the layover areas outside of the building footprint contain more useful information on the type of building damage. the backscattering coefficient value will change most significantly in those areas where the buildings are totally destroyed. Therefore, block-based building damage assessment was adopted in this paper with the aim of solving the limitation of damage assessment on a single-building scale. The scales of the block object directly influence the

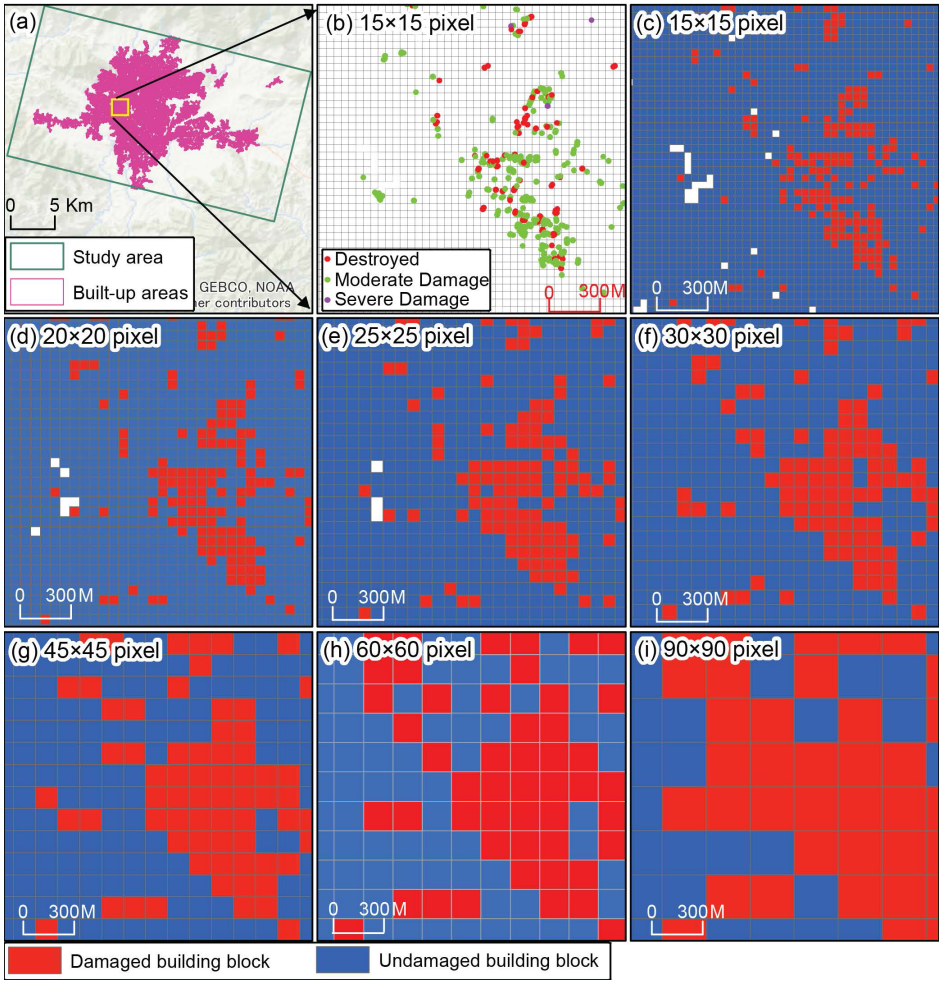

Fig. 5. Result of block object ground truth data (GTD) generation. (a) Study area and the extracted built-up areas. (b) The three classes for individual building scale as GTD [24]. (c)-(i) The block-scale object GTD in 15 × 15 pixel, 20 × 20 pixel, 25 × 25 pixel, 30 × 30 pixel, 45 × 45 pixel, 60 × 60 pixel,90 × 90 pixel respectively.

final accuracy of building damage assessment. To evaluate the impact of changing scales on the building damage class separability, block object was calculated at 7 different scales (15 × 15 pixels, 20 × 20 pixels, 25 × 25 pixels, 30 × 30 pixels, 45 × 45 pixels, 60 × 60 pixels, and 90 × 90 pixels). First, we used a value of 1515 pixels for the generation of tile-based block object, and then we gradually increased this value. Subsequent to the BA area extraction shown in **Fig. 5(a)**, the 3-class GTD of affected buildings, shown in **Fig. 5(b)** and provided by the United Nations Institute for Training and Research (UNITAR) Operational Satellite Applications Programme (UNOSAT), was extrapolated to create a sample database with all objects assigned either as damaged building block (DBB) or undamaged building block (UBB). Block objects containing at least one damaged building (destroyed, severely damaged, and/or moderately damaged building) was labeled as DBB and all others as UBB. The results of the building block GTD (15 × 15 pixels) are shown in **Fig. 5(c)**. The same method was applied to the blocks of other scales (20 × 20 pixels, 25 × 25 pixels, 30 × 30 pixels, 45 × 45 pixels, 60 × 60 pixels, and 90 × 90 pixels) to generate the multiscale building block GTD as shown in **Figs. 5(d)-(i)**.

3.3. Calculation of Image Object Metrics

This section presents all the metrics used in this study. The metrics were calculated within the building block obtained in the previous step. In addition to the frequently used co-polarization backscattering coefficient, three new polarimetric features were calculated per image object: cross-polarization backscattering coefficient, cross polarization ratio, and modified total scattering power. The cross-polarization ratio (CPR) was defined as the ratio between cross-polarization (σ_{HV}) and co-polarization (σ_{HH}). The modified total scattering power (SPAN*), which represents the brightness of an illuminated object, was defined as the sum of the scattering power of co-polarization and cross-polarization. The dualpolarimetric ALOS2/PALSAR2 data can be represented in forms of the covariance matrix (C2). By applying the H-2-alpha decomposition [25], we calculated the dual-pol target parameters entropy (H), anisotropy (A), alpha angle (α), and Shannon entropy [26]. Also, by performing the Raney decomposition [27], we obtained the modified double bounce scattering (Dbl), odd scattering (Odd), and random scattering (Rnd). In addition, the reflection symmetry metric, which represents the unnormalized correla-

Table 2. Overview of features used to identify earthquake induced building damage adopted in this study. Number marked with star indicates the number of features calculated from the ALOS-2/PALSAR-2 image acquired on May 2, 2015.

	Tested features	Number of features
Polarimetric	Entropy,Anisotropy,alpha, Shannon entropy	4*
	Backscattering coefficient (σ^*_{HH},σ^*_{HV}),$\langle S_{HV}S^*_{HH}\rangle$,$\langle S_{HH}S^*_{HV}\rangle$	4*
	$Raney_{Rnd}$, $Raney_{Odd}$, $Raney_{Dbl}$	3*
	Backscattering coefficient (σ_{HH},σ_{HV})	2
	Cross polarization ratio(CPR), SPAN	2
Texture	$GLCM_{0^\circ}.HH.(Mean,Cor.,Con.,ASM,MP,Var.,Hom.,Ene.,Dis.)$	9
	$GLCM_{45^\circ}.HH.(Mean,Cor.,Con.,ASM,MP,Var.,Hom.,Ene.,Dis.)$	9
	$GLCM_{90^\circ}.HH.(Mean,Cor.,Con.,ASM,MP,Var.,Hom.,Ene.,Dis.)$	9
	$GLCM_{135^\circ}.HH.(Mean,Cor.,Con.,ASM,MP,Var.,Hom.,Ene.,Dis.)$	9
	$GLCM_{0^\circ}.HV.(Mean,Cor.,Con.,ASM,MP,Var.,Hom.,Ene.,Dis.)$	9
	$GLCM_{45^\circ}.HV.(Mean,Cor.,Con.,ASM,MP,Var.,Hom.,Ene.,Dis.)$	9
	$GLCM_{90^\circ}.HV.(Mean,Cor.,Con.,ASM,MP,Var.,Hom.,Ene.,Dis.)$	9
	$GLCM_{135^\circ}.HV.(Mean,Cor.,Con.,ASM,MP,Var.,Hom.,Ene.,Dis.)$	9
	$GH_{HH}.(DataR.,Var.,Ske.,Mean)$	4
	$GH_{HV}.(DataR.,Var.,Ske.,Mean)$	4
	$Gabor_{HH}$, $Gabor_{HV}$	2
	Speckle divergence	1
Color	Hue, Saturation, Value, Light	4

tion between co-polarization and cross-polarization, was used in this study [27, 28].

To quantify surface textures, a variety of derivatives of the gray level co-occurrence matrix (GLCM) that had been evaluated in previous earthquake-induced building damage assessment studies were adopted for this study. These are contrast (Con.), correlation (Cor.), energy (Ene.), angular second moment (ASM.), maximum probability (MP.), variance (Var.), homogeneity (Hom.), dissimilarity (Dis.), and mean. The open source sentinel toolbox [29] was used in this study to calculate GLCM features at directions of 0°, 45°, 90°, 135° for co-polarization and cross-polarization, respectively. The Gabor filter-based features [30] and occurrence Matrix-based texture features (data range, variance, skewness, and mean) (Anys et al., 1994). as well as speckle divergence [23] were also taken into account for this evaluation.

With the development of high-resolution polarimetric SAR imaging techniques, it is available for us to obtain color information from the pseudo-color or false color of polarimetric SAR images. The application of color features follows the same concept as the texture features by exploiting statistical properties and the relationship within a pixel window. More importantly, the color information represented in false color polarimetric images has already provided promising results in earthquake-induced landslide mapping [31] and other applications [32]. Therefore, we considered integrating the color features derived from the most famous hue saturation-value/intensity (HSV) color space model and hue-light-saturation (HLS) color space model to build damage assessment. Considering dual-pol SAR data, the two polarization backscattering coefficient images were used to directly generate pseudo color imagery. The color composite in the image represents σ_{HH} in red, σ_{HV} in green, and σ_{HH}/σ_{HV} in blue. Together with the texture metrics and polarimetric metrics, a total of 102 features were calculated for the ultrafine mode SAR imagery and fine mode SAR imagery, respectively (**Table 2**).

3.4. Random Forests

The Random Forest machine learning algorithm has already been demonstrated to be powerful in fields such as biomedicine [33, 34], environmental engineering [16, 17], and Earth observation [35, 36] since the concept of ensemble decision trees was proposed [37]. The performance of the traditional decision tree is highly dependent on the dataset and often generates rather low classification accuracies [38] due to the complexity of remote sensing data. However, the RF algorithm classifies by generating a number of decision trees. It does this based on bootstrap sampling and random feature combinations strategy [37], which greatly increases the robustness and performance of classification. In this work, we mainly used the Random Forest tools implemented in the Salford Predictive Modeler software [39].

Damaged buildings accounted for only minor fractions of our test area, as is common after earthquake disasters. This situation leads to an imbalance between DBB and UBB, and it potentially introduces a bias towards the over-representation of UBB in the classification. Such biases are undesirable in earthquake damage mapping because an overestimation or underestimation of the affected areas will generally mislead the disaster response and the associated hazard and risk assessments. To alleviate the error induced by class imbalance, a balanced class weight which increases the weighting of small classes to equal that of the largest target class was adopted. To quantitatively rank the contribution of different features in the

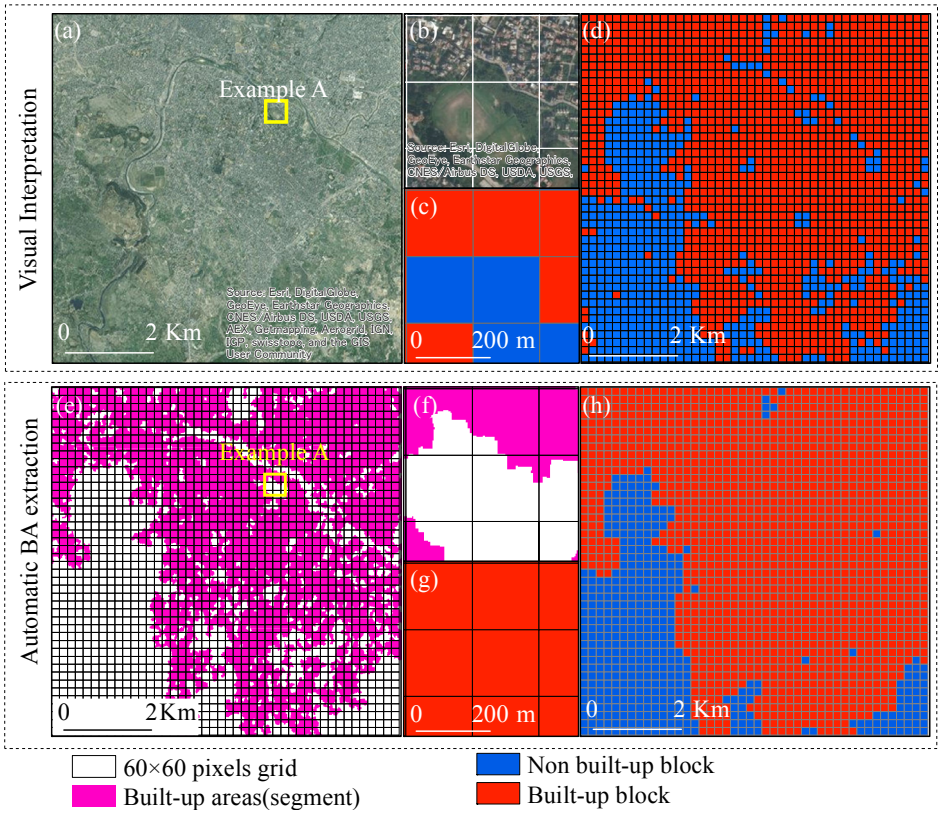

Fig. 6. The process of accuracy validation for the extracted BA areas. (a) VHR optical image. (b) Magnified VHR optical image in example A. (c) Visually interpreted BA blocks in example A. (d) Visually interpreted BA results in the whole evaluation area. (e) The automatic extracted BA (segments) in evaluation area. (f) Magnified BA (segments) in example A. (g) Interpolated BA blocks in example A. (d) Interpolated BA blocks in the whole evaluation area.

final damage classification, a RF-based variable importance (VI) [40] was employed to assess the metrics at the same test site on 7 different scales.

4. Results and Discussion

4.1. BA Extraction Accuracy Assessment

To validate the accuracy of the extracted BA, an area located in the southeast of the study area was selected for quantitative assessment, as seen in **Fig. 4(d)**. The GTD of the BA was constructed based on the visual interpretation of the VHR optical image, provided by DigitalGlobe and shown in **Fig. 6(a)**. First, the evaluation area was split into 60 × 60-pixel grid objects (**Fig. 6(e)**), and the visual interpretation was performed for each object. An object was identified as a BA if numerous buildings were observed within it; otherwise, the object was identified as a non-BA. One example of the interpretation process is shown in **Figs. 6(b)** and **6(c)**, and the interpreted BA in the evaluation area is shown in **Fig. 6(d)**. For comparison with the GTD of the BA, we interpolated, using the proposed method, the automatic extracted BA (see **Fig. 6(e)**) into a 60 × 60-pixel grid object scale, as seen in **Fig. 6(h)**. All the 60 × 60-pixel grid objects that interact with the automatic extracted BA were classified as a BA. One example of the interpolation process can be seen in **Figs. 6(f)** and **6(g)**.

The accuracy assessment is summarized in **Table 3** and **Fig. 5**. The results show that the BA was identified with an overall accuracy of 90.7% and a kappa coefficient of 0.776 for the validated areas. For the test site, promising results were achieved while errors occurred mainly in the context of BA which were highly interspersed with bridges, parks, and greenhouses. This is because the scattering characteristics of the dispersive objects are quite similar to those of the BA, so the dispersive objects are easily misclassified. However, since those objects only constitute a small part of the total study area, it can be said that the model worked well.

4.2. Variable Importance Ranking and Effects of Scale on Classification Accuracy

Variable importance provides us with a simple way to compare the contribution of different features derived from the SAR image for classification accuracy, and this can also help us to analyze the causal relationship between SAR image characteristics and the type of building damage. Unsurprisingly, features related to polarimetric information and texture information turned out to be the most important ones for all test scales (**Table 4**). The random scattering metric ($Raney_{Rnd}$) that depicts the scattering re-

Table 3. Accuracy assessment of the extracted built-up area (BA).

		Classified result			
		BA block	Non-BA block	Total	P.A.(%)
GTD	BA block	1370	28	1398	97.8
	Non-BA block	164	506	670	75.5
	Total	1534	534		Kappa coefficient=0.776
	U.A.(%)	89.3	94.8		Overall accuracy=90.7%

Table 4. The 20 object metrics with the highest average variable importance rank among four tested scales. Blue fonts represent color metrics, green fonts represent polarimetric metrics, and the black fonts represent texture metrics.

15×15 pixel)		30×30 pixel		60×60 pixel		90×90 pixel	
Feature	Score	Feature	Score	Feature	Score	Feature	Score
$Raney_{Rnd}$	100.0	$\langle S_{HV}S^*_{HH}\rangle$	100.0	$GLCM_{135°.HH.MP}$	100.0	σ_{HH}	100.0
CPR	87.6	σ_{HH}	95.3	$Gabor_{HH}$	19.4	$GLCM_{0°.HV.MP}$	57.9
Anisotropy	75.2	$\langle S_{HH}S^*_{HV}\rangle$	86.8	$\langle S_{HH}S^*_{HV}\rangle$	12.1	$GLCM_{45°.HV.Vari}$	54.9
light	75.2	$Raney_{Rnd}$	51.4	$Gabor_{HV}$	11.1	$Raney_{Rnd}$	54.5
$\langle S_{HV}S^*_{HH}\rangle$	71.2	$Entropy_{Shannon}$	38.4	σ_{HH}	10.2	$GLCM_{0°.HV.Mean}$	53.6
$Gabor_{HH}$	69.0	$Gabor_{HH}$	36.3	σ_{HV}	8.0	$GLCM_{90°.HV.Vari}$	52.4
Vaule	62.6	$GLCM_{45°.HV.Mean}$	34.8	$Raney_{Rnd}$	7.0	$\langle S_{HH}S^*_{HV}\rangle$	51.4
σ_{HH}	61.2	$GLCM_{135°.HV.Mean}$	35.3	$\langle S_{HV}S^*_{HH}\rangle$	7.0	$GH_{HV.Vari}$	45.8
$GLCM_{45°.HH.ASM}$	60.1	$GLCM_{90°.HV.Mean}$	31.7	$GLCM_{45°.HH.MP}$	6.5	$GH_{HV.DataRange}$	45.8
$GLCM_{0°.HH.Homo}$	55.5	$GLCM_{0°.HH.Corre}$	30.2	$GLCM_{135°.HV.Vari}$	6.4	$GLCM_{0°.HV.ASM}$	44.4
σ^*_{HV}	53.4	$GLCM_{90°.HV.Corre}$	27.2	$GH_{HV.Vari}$	6.4	$Gabor_{HH}$	44.2
$Raney_{Dbl}$	52.9	$GLCM_{0°.HV.Mean}$	25.0	$Entropy_{Shannon}$	6.3	$GLCM_{90°.HV.MP}$	43.4
$GLCM_{0°.HH.MP}$	52.7	σ_{HV}	25.6	$GLCM_{0°.HH.MP}$	5.8	$GLCM_{90°.HV.Mean}$	41.0
Entropy	50.1	$Raney_{Odd}$	26.8	$GH_{HV.Mean}$	5.8	$GLCM_{90°.HV.Energy}$	40.2
$GLCM_{45°.HH.Homo}$	45.3	$GLCM_{135°.HH.Mean}$	26.4	$GLCM_{90°.HH.MP}$	5.5	$GLCM_{0°.HV.Homo}$	40.1
$Raney_{Odd}$	43.6	$Gabor_{HV}$	26.7	$GLCM_{90°.HV.Mean}$	5.1	$GLCM_{45°.HV.MP}$	39.4
$GLCM_{0°.HH.Corre}$	41.7	$Raney_{Dbl}$	23.7	$GLCM_{90°.HV.Vari}$	4.9	$GLCM_{0°.HV.Energy}$	39.0
$GLCM_{0°.HH.ASM}$	38.3	σ_{HV}	22.6	$GLCM_{0°.HV.MP}$	4.9	$GLCM_{135°.HV.Vari}$	38.8
$GLCM_{45°.HH.Mean}$	37.6	$GLCM_{90°.HV.Corre}$	21.3	$GLCM_{90°.HV.MP}$	4.9	$GH_{HV.Mean}$	37.8
$\langle S_{HH}S^*_{HV}\rangle$	37.6	$GLCM_{0°.HV.Vari}$	21.4	$GLCM_{135°.HH.ASM}$	4.6	$GLCM_{135°.HH.ASM}$	37.1

sponse from the randomly distributed targets showed a particularly high variable importance (VI) value. The reflection symmetry metric ($S_{HV}S^*_{HH}$) also contributed significantly to the classification accuracy, which indicates that the reflection symmetry characteristics of the DBB and the UBB are different. However, in most cases, their relative variable importance increased with larger block scales (**Table 4**). In general, GLCM MP., Mean., Vari., Homo., and Corri., also had relatively high VI values. However, the VI rankings of the most important textural features exhibited a large degree of variability among the different block scales. The co-polarization-guided GLCM MP., ASM., to reduce the OOB error in the 15 × 15-pixel scale and 60 × 60-pixel scale tests, and it largely outperformed the cross-polarization-guided GLCMs. The cross-polarization-guided GLCMs Vari. and Mean. helped to reduce the OOB error in the 30 × 30-pixel scale and 90 × 90-pixel scale tests, and they largely outperformed the co-polarization-guided GLCMs. Furthermore, the ranking of the texture features increased along with the increase in block scales, indicating that the texture information makes it easier to distinguish the damaged blocks in the larger scales. Although the optimal choice of the texture measures depends to a certain degree on the application, it is interesting to note that previous research highlighted the co-polarization-guided GLCMs Homo., Vari., and Ent. as particularly useful features for collapsed building identification [12, 41]. The present study showed that the cross-polarization-guided GLCMs are even more useful and should therefore be considered.

Color features displayed rather contrary behavior and generally contributed little to increased classification accuracy. Only for smaller block scales, which have blocks that are closer to the size of a single building, the light and value features were selected by the selection procedure. The color information has been reported to significantly improve the accuracy of polarization SAR classification [32] and to be useful in landslide detection [31], but it provided little additional information within the tested sample-based framework. On the whole, the abilities of the texture and color features to distinguish were not as good in this study as those of the polarimetric features. One possible reason is that the scattering process of radar is very sensitive to varieties in the orientation, size, and shape of buildings, and the difference of buildings with different damage degree represented in SAR image is dif-

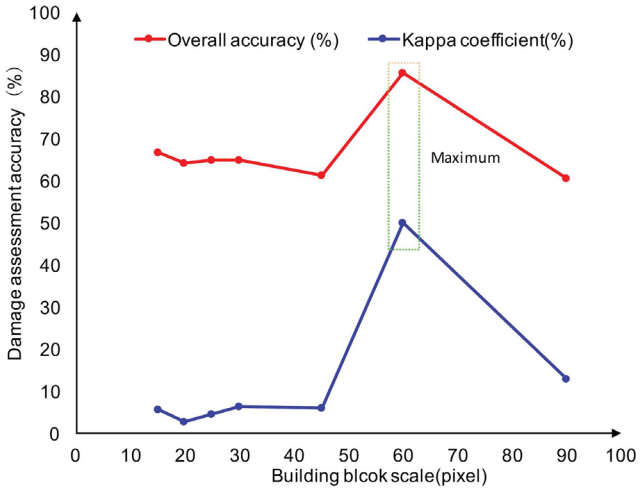

Fig. 7. The effect of block scale on the final accuracy of building damage assessment.

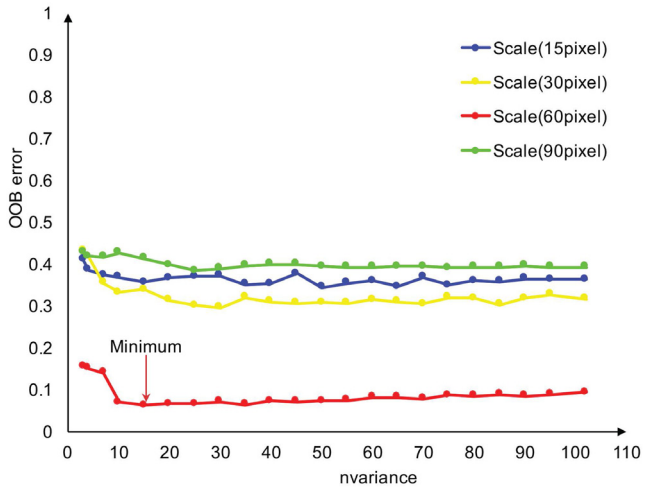

Fig. 8. Evaluation of feature reduction using block-object scales of 15 × 15, 30 × 30, 60 × 60, and 90 × 90 pixels.

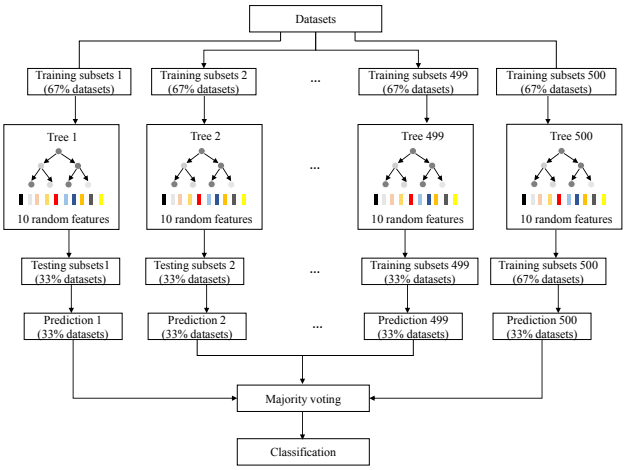

Fig. 9. The flowchart of random forest algorithm used in this study for accuracy assessment.

ficult to describe using a simple visual model due to the limitation of the relatively low resolution of SAR images.

On the other hand, the effect of block scale on classification accuracy was also investigated, as shown in **Fig. 7**, in order to find an optimum block scale for building damage classification. The results show that the scale of 60 × 60 pixels has the best performance, with an overall accuracy of 85.8% and a kappa coefficient of 0.5. This is also in accordance with our previous assumption. The reasons are as follows. 1) The ideal block object should contain a number of buildings and the interstitial area between buildings so that the typical radar scattering behavior may be grasped from the viewpoint of block level. However, the small scale block object may only be able to contain the radar scattering information of pure buildings or pure interstitial area between buildings, which will decrease the accuracy of block object classification. Satisfying results can be achieved if the damage is assessed with a bigger size of block object, somehow averaging the unreliable results of small-scale block objects. 2) Larger object scales generally generate fewer and larger-sized sample objects, and the precision of the block-object GTD will decrease along with the increase of the object scale. Based on these two reasons, the medium-scale object (60 × 60 pixels) can balance the radar scattering characterization and the block-object GTD precision, and it had the best results.

4.3. The Effects of Variable Number on the Classification Accuracy

Developing a model with high classification accuracy is possible by utilizing many kinds of features. However, the applicability of this strategy is restricted by the high redundancy and time costs. For real applications such as quick disaster response, exploring the optimal strategy of achieving the ideal result using the smallest set of features is important. Based on the above mentioned variable importance ranking, a predictive accuracy assessment was performed by employing a gradually decreasing number of features. As shown in **Fig. 8**, on average, only about one-fifth of the pre-selected features were detected as useful, and the OOB error reached a minimum when 15 features were used in a 60 × 60-pixel scale. The 15 features are the top 15 features for the 6060 pixels in **Table 4**, namely, $GLCM_{135°.HH.MP}$, $Gabor_{HH}$, $\langle S_{HH}S^*_{HV}\rangle$, $Gabor_{HV}$, σ_{HH}, σ_{HV}, $Raney_{Rnd}$, $\langle S_{HV}S^*_{HH}\rangle$, $GLCM_{45°.HH.MP}$, $GLCM_{135°.HV.Vari}$, $GH_{HV.Vari}$, $Entropy_{Shannon}$, $GLCM_{0°.HH.MP}$, $GH_{HV.Mean}$, $GLCM_{90°.HH.MP}$, respectively. In most cases, the OOB error remained basically stable or increased if all variables were used. In the tests involving the 60 × 60-pixel and 90 × 90-pixel scales in particular, many of the features provided only minor further enhancements or were even detrimental. More importantly, the test revealed that even a small number of variables are also capable of achieving high accuracy; most of the preselected features are redundant or provide limited useful information and should therefore be excluded.

Table 5. Accuracy assessment results for the Random Forest classifier.

Random Forest classifier					
		UBB	DBB	Total	P.A.(%)
	UBB	4691	320	5011	93.6
GTD	DBB	36	528	564	93.6
	Total	4727	848		Kappa coefficient=0.885
	U.A.(%)	99.2	62.2		Overall accuracy=93.6%

Table 6. Accuracy assessment results for the k-nearest neighbor classifier.

k-nearest neighbor classifier					
		UBB	DBB	Total	P.A.(%)
	UBB	4922	89	5011	98.2
GTD	DBB	383	181	564	32.1
	Total	5305	270		Kappa coefficient=0.40
	U.A.(%)	92.8	33.0		Overall accuracy=91.5%

4.4. Accuracy Assessment

In this study, we did not manually determine the training sample or areas because the final accuracy would be highly affected by a manually selected training sample. In order to avoid this uncertainty, we employed bootstrap sample-based out of bag (OOB) testing to create the training sets and validation sets automatically. The number of trees (t) and the number of features used to divide in each node (n) in this study were empirically set to 500 and 10, respectively. 10 features from **Table 4** were randomly selected for the construction of decision tree 1, 63% of the original datasets were randomly selected as the training sets, and the remaining 37% datasets were used as test sets. This process was independently repeated 500 times to construct 500 trees. The prediction of each validation dataset from each independent test was used for a majority vote to get the final predication. The details of the Random Forest algorithm can be seen in **Fig. 9**. It has already been widely acknowledged that the results of the OOB testing are much more reliable and stable than when the traditional manual sample selection process is used. According to the above analysis, the 60 × 60-pixel scale with 15 features generates the best performance, so it was selected for accuracy assessment. In order to demonstrate the superiority of the RF model for classification, the widely used k-nearest neighbor classifier (KNN) was also tested for comparison. In the confusion matrix shown in **Tables 5** and **6**, it is easily seen that for the RF models, overall accuracy (93.6%) and the kappa coefficient (0.71) are higher than those for the KNN model (91.5% and 0.40, respectively). A significant underestimation of damaged blocks was observed in the KNN model. In contrast, the soft decision of the RF classifier showed a significant improvement and yielded balanced results. If one compares the GTD map (**Fig. 10(a)**), the RF model-based damage map (**Fig. 10(b)**), and KNN model-based damage map (**Fig. 10(c)**), one can easily see that the building blocks in the southern part of our study area are overestimated as damaged building blocks. The building density in the misclassified areas is much lower than that in the correctly classified areas. Thus, the radar characteristic is quite different from that in the correctly classified areas and likely to be misclassified.

5. Conclusion

Previously presented methodologies for earthquake-induced building damage assessment from SAR images have been highly dependent on the available datasets, including preseismic SAR data and building footprint data, and a time-consuming threshold determination. This dependency on available datasets has made it difficult to use the resulting assessments in other real applications.

To improve the applicability of the previous methodologies, this study explored the integration of two technologies, i.e., speckle divergence-based object analysis and the Random Forest-based machine learning framework, for built-up area extraction and object-based building damage estimation. Two ALOS-2/PALSAR-2 dual polarimetric SAR datasets of the affected areas acquired soon after the 2015 Nepal earthquake were evaluated to determine the effective features, the influence of the object scale, and the effects of the feature reduction on predictive accuracy. Although the optimal set of features varies distinctively from case to case, a number of polarimetric, texture, and color features proved to be useful. The color information derived from the pseudo color imagery provided only a little complementary information in terms of distinguishing the type of building damage while the random scattering metric and the reflection symmetry metric that originated from the dual polarimetric image in this paper provided more significant enhancements. This study also showed that the newly introduced, cross-polarization-guided GLCMs are even more useful and thus worthy of attention. In general, the color features are not as good as the polarimetric and texture features in terms of distinguishing types of damage. Our results indicate that feature reduction leads to improved estimation, but they also indicate that not all significant

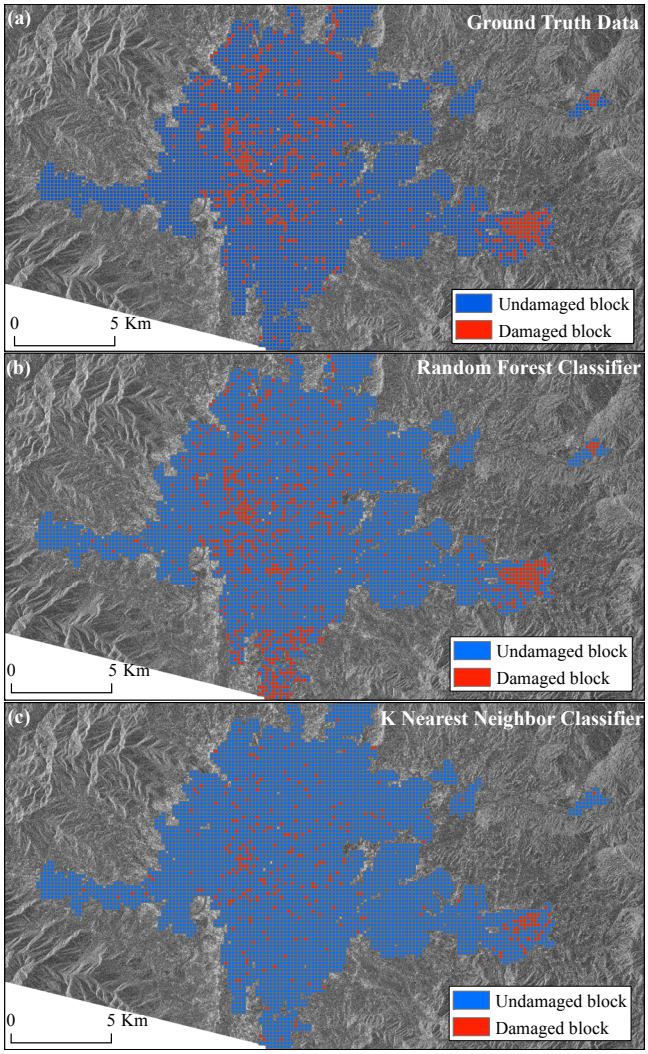

Fig. 10. The comparison of the block-object GTD (60 × 60 pixel) and the classification result. (a) Block-object ground truth data (60 × 60 pixel). (b) RF classifier based damage classification result. (c) KNN classifier based damage classification result.

features can be fully exploited with one particular segmentation scale. In summary, the RF classifier provided relatively high overall accuracies, up to 93% with a kappa coefficient of 0.885 when the 60×60-pixel scale and 15 features are adopted, while the comparative test using the k-nearest neighbor classifier achieved overall accuracies of up to 91.5% with a kappa coefficient of 0.40, demonstrating that the soft decision of the RF classifier affords a significant improvement in terms of balancing the correct classification. However, it seems that the range of potentially useful features for earthquake-induced building damage mapping has still not been fully exploited; other kinds of SAR datasets, such as the fully polarimetric SAR dataset, should be used to explore the physical scattering mechanism of radar in the built-up areas affected by earthquake.

One of the most important advantages of the proposed framework is its high applicability. One post-event remote sensing image and a small portion of ground truth data were sufficient for an efficient performance of the RF classifiers. In most practical situations, such data will be available. In situations in which more data, such as pre-event imagery or remote sensing data from any other source, are available, the proposed framework can accommodate a large variety of additional datasets and object metrics, and these may be used to further increase mapping accuracies. In summary, the framework presented in this paper provides a general approach to mapping the overall area affected by earthquake. It also has to be noted that, at this point, we have only explored the technical aspects of the damage mapping with the help of ground truth data; in real disaster responses, the ground truth data cannot be expected. In order to quickly achieve damage mapping without ground truth data, the current architecture will require further enhancements. Furthermore, for quick disaster responses in the future, there will be a strong need for a streamlined building-damage estimation system implemented on a desktop computer.

Acknowledgements

We would like to thank the Japan Aerospace Exploration Agency (JAXA) for providing our dataset of SAR imagery. This work was supported by JSPS KAKENHI Grant Number 25242035, the JST CREST Project, and the China Scholarship Council (CSC).

References:

[1] S. A. Bartels and M. J. Vanrooyen, "Medical complications associated with earthquakes," 2012.

[2] M. Dou, J. Chen, D. Chen, X. Chen, Z. Deng, X. Zhang, K. Xu, and J. Wang, "Modeling and simulation for natural disaster contingency planning driven by high-resolution remote sensing images," Future Generation Computer Systems, Vol.37, pp. 367–377, 2014.

[3] K. Saito, R. J. S. Spence, C. Going, and M. Markus, "Using High-Resolution Satellite Images for Post-Earthquake Building Damage Assessment: A Study Following the 26 January 2001 Gujarat Earthquake," 2004.

[4] F. Yamazaki, Y. Yano, and M. Matsuoka, "Visual damage interpretation of buildings in Bam city using QuickBird images following the 2003 Bam, Iran, earthquake," 2005.

[5] M. Matsuoka, H. Miura, S. Midorikawa, and M. Estrada, "Extraction of urban information for seismic hazard and risk assessment in Lima, Peru using satellite imagery," Journal of Disaster Research, Vol.8, No.2, pp. 328–345, 2013.

[6] T. Hoshi, O. Murao, K. Yoshino, F. Yamazaki, and M. Estrada, "Post-disaster urban recovery monitoring in pisco after the 2007 peru earthquake using satellite image," Journal of Disaster Research, Vol.9, No.6, pp. 1059–1068, 2014.

[7] H. Gokon, S. Koshimura, and M. Matsuoka, "Object-based method for estimating Tsunami-induced damage using TerraSAR-X data," Journal of Disaster Research, Vol.11, No.2, pp. 225–235, 2016.

[8] M. Matsuoka and M. Estrada, "Development of earthquake-induced building damage estimation model based on ALOS/PALSAR observing the 2007 Peru earthquake," Journal of Disaster Research, Vol.8, No.2, pp. 346–355, 2013.

[9] M. Matsuoka, S. Mito, S. Midorikawa, H. Miura, L. G. Quiroz, Y. Maruyama, and M. Estrada, "Development of Building Inventory Data and Earthquake Damage Estimation in Lima , Peru for Future Earthquakes," Journal of Disaster Research, Vol.9, No.6, pp. 1032–1041, 2014.

[10] X. Li, H. Guo, L. Zhang, X. Chen, and L. Liang, "A New Approach to Collapsed Building Extraction Using RADARSAT-2 Polarimetric SAR Imagery," IEEE Geoscience and Remote Sensing Letters, Vol.9, No.4, pp. 677–681, 2012.

[11] L. Shi, W. Sun, J. Yang, P. Li, and L. Lu, "Building Collapse Assessment by the Use of Postearthquake Chinese VHR Airborne SAR," IEEE Geoscience and Remote Sensing Letters, Vol.12, No.10, pp. 2021–2025, 2015.

[12] F. Dell'Acqua, C. Bignami, M. Chini, G. Lisini, D. A. Polli, and S. Stramondo, "Earthquake damages rapid mapping by satellite remote sensing data: L'Aquila april 6th, 2009 event," IEEE Journal of Selected Topics in Applied Earth Observations and Remote Sensing, Vol.4, No.4, pp. 935–943, 2011.
[13] L. Zhao, J. Yang, P. Li, L. Zhang, L. Shi, and F. Lang, "Damage assessment in urban areas using post-earthquake airborne PolSAR imagery," International Journal of Remote Sensing, Vol.34, No.24, pp. 8952–8966, 2013.
[14] B. Guo, R. I. Damper, S. R. Gunn, and J. D. B. Nelson, "A fast separability-based feature-selection method for high-dimensional remotely sensed image classification," Pattern Recognition, Vol.41, No.5, pp. 1670–1679, 2008.
[15] L. Breiman, "Random forests," Machine Learning, Vol.45, No.1, pp. 5–32, 2001.
[16] S. A. Naghibi, H. R. Pourghasemi, and B. Dixon, "GIS-based groundwater potential mapping using boosted regression tree, classification and regression tree, and random forest machine learning models in Iran," Environmental Monitoring and Assessment, Vol.188, No.1, pp. 1–27, 2016.
[17] O. Rahmati, H. R. Pourghasemi, and A. M. Melesse, "Application of GIS-based data driven random forest and maximum entropy models for groundwater potential mapping: A case study at Mehran Region, Iran," Catena, Vol.137, pp. 360–372, 2016.
[18] M. Belgiu and L. Drgu, "Random forest in remote sensing: A review of applications and future directions," ISPRS Journal of Photogrammetry and Remote Sensing, Vol.114, pp. 24–31, 2016.
[19] A. L. Mitchell, I. Tapley, A. K. Milne, M. L. Williams, Z. S. Zhou, E. Lehmann, P. Caccetta, K. Lowell, and A. Held, "C- and L-band SAR interoperability: Filling the gaps in continuous forest cover mapping in Tasmania," Remote Sensing of Environment, Vol.155, pp. 58–68, 2014.
[20] A. Solikhin, V. Pinel, J. Vandemeulebrouck, J. C. Thouret, and M. Hendrasto, "Mapping the 2010 Merapi pyroclastic deposits using dual-polarization Synthetic Aperture Radar (SAR) data," Remote Sensing of Environment, Vol.158, pp. 180–192, 2015.
[21] M. Shakya and C. K. Kawan, "Reconnaissance based damage survey of buildings in Kathmandu valley: An aftermath of 7.8Mw, 25 April 2015 Gorkha (Nepal) earthquake," Engineering Failure Analysis, Vol.59, No.April, pp. 161–184, 2016.
[22] E. Agency, "April 15, 2016 Japan Aerospace Exploration Agency," tech. rep., 2016.
[23] T. Esch, M. Thiel, A. Schenk, A. Roth, A. Müller, and S. Dech, "Delineation of Urban footprints from TerraSAR-X data by analyzing speckle characteristics and intensity information," IEEE Transactions on Geoscience and Remote Sensing, Vol.48, No.2, pp. 905–916, 2010.
[24] UNITAR, tech. rep., 2015, http://www.unitar.org/unosat/maps/NPL [accessed April 12, 2015]
[25] C. N. Koyama, K. Schneider, and M. Sato, "Development of a Biomass Corrected Soil Moisture Retrieval Model for Dual-Polarization Alos-2 Data Based on Alos / Palsar and Pi-Sar-L2 Observations," IGASS, No.April 2012, pp. 1316–1319, 2015.
[26] J. Betbeder, S. Rapinel, S. Corgne, E. Pottier, and L. Hubert-Moy, "TerraSAR-X dual-pol time-series for mapping of wetland vegetation," ISPRS Journal of Photogrammetry and Remote Sensing, Vol.107, pp. 90–98, 2015.
[27] F. Nunziata, M. Migliaccio, S. Member, and C. E. Brown, "Re fl ection Symmetry for Polarimetric Observation of Man-Made Metallic Targets at Sea," IEEE Journal of Oceanic Engineering, Vol.37, No.3, pp. 384–394, 2012.
[28] D. South, D. Velotto, C. Bentes, B. Tings, and S. Lehner, "First Comparison of Sentinel-1 and TerraSAR-X Data in the Framework of Maritime Targets," IEEE Journal of Oceanic Engineering, pp. 1–14, 2016.
[29] ESA, 2015, http://step.esa.int/main/download/ [accessed May 12, 2016]
[30] M. Tuceryan, M. Tuceryan, A. K. Jain, and A. K. Jain, "The Handbook of Pattern Recognition and Computer Vision (2nd Edition), Texture Analysis," Pattern Recognition, pp. 207–248, 1998.
[31] N. Li, R. Wang, Y. Deng, Y. Liu, B. Li, C. Wang, and T. Balz, "Unsupervised polarimetric synthetic aperture radar classification of large-scale landslides caused by Wenchuan earthquake in hue-saturation-intensity color space," Journal of Applied Remote Sensing, Vol.8, No.1, p. 083595, 2014.
[32] S. Uhlmann and S. Kiranyaz, "Classification of dual- and single polarized SAR images by incorporating visual features," ISPRS Journal of Photogrammetry and Remote Sensing, Vol.90, pp. 10–22, 2014.
[33] V. Lempitsky, M. Verhoek, J. A. Noble, and A. Blake, "Random forest classification for automatic delineation of myocardium in real-time 3D echocardiography," in Lecture Notes in Computer Science (including subseries Lecture Notes in Artificial Intelligence and Lecture Notes in Bioinformatics), Vol.5528, pp. 447–456, 2009.
[34] B. R. Smith, K. M. Ashton, A. Brodbelt, T. Dawson, M. D. Jenkinson, N. T. Hunt, D. S. Palmer, and M. J. Baker, "Combining random forest and 2D correlation analysis to identify serum spectral signatures for neuro-oncology," The Analyst, pp. 3668–3678, 2016.
[35] JiSoo Ham, Yangchi Chen, Melba M. Crawford, and J. Ghosh, "Investigation of the Random Forest Framework for\rClassification of Hyperspectral Data," IEEE Transactions on Geoscience and Remort Scensing, Vol.43, No.3, pp. 492–501, 2005.
[36] B. Koch, "Status and future of laser scanning, synthetic aperture radar and hyperspectral remote sensing data for forest biomass assessment," ISPRS Journal of Photogrammetry and Remote Sensing, Vol.65, No.6, pp. 581–590, 2010.
[37] L. Breiman, "Random forests," Machine Learning, Vol.45, No.1, pp. 5–32, 2001.
[38] L. Breiman, "Technical note: Some properties of splitting criteria," Machine Learning, Vol.24, pp. 41–47, 1996.
[39] Dan Steinberg, "Salford Systems," 1983.
[40] K. K. Nicodemus, J. D. Malley, C. Strobl, and A. Ziegler, "The behaviour of random forest permutation-based variable importance measures under predictor correlation," BMC bioinformatics, Vol.11, p. 110, 2010.
[41] D. Aldo, F. Dell, P. Gamba, and G. Lisini, "Earthquake damage assessment from post-event only radar satellite data," October 2015.

Name:
Yanbing Bai

Affiliation:
Ph.D. Student, Graduate School of Engineering, Tohoku University

Address:
Aoba 468-1, Aramaki, Aoba-ku, Sendai, 980-0845, Japan

Brief Career:
2011-2014 Master of Science, School of Earth and Space Sciences, Peking University, China
2014- PhD student, Graduate School of Engineering, Tohoku University, Japan

Selected Publications:
• N. Wang, Q. Qin, L. Chen, and Y. Bai, "Dynamic monitoring of coalbed methane reservoirs using Super-Low Frequency electromagnetic prospecting," International Journal of Coal Geology, Vol.127, pp. 24-41, 2014.
• Y. Bai, B. Adriano, E. Mas, G. Hideomi, and S. Koshimura, "Building damaged detection using ALOS-2/PALSAR-2 dual polarimetric SAR intensity imagery," In The APRU symposium series on Multi-hazards around the Pacific Rim, pages CD-ROM, 2015.
• Y. Bai, B. Adriano, E. Mas, and S. Koshimura, "Building damage assessment using post-event dual polarimetric SAR. In the 2016 Tohoku shibu conference, pages CD-ROM, 2016.
• Y. Bai, B. Adriano, E. Mas, and S. Koshimura, "Developing a methodology for building damage mapping using only post-event dual-polarimetric SAR data – Case study from the 2015 Nepal earthquake. In the 2016 Asia Oceania Geosciences Society conference, pages CD-ROM, 2016.

Academic Societies & Scientific Organizations:
• Japan Society of Civil Engineers (JSCE)

Name:
Bruno Adriano

Affiliation:
Postdoctoral Researcher, International Research Institute of Disaster Science (IRIDeS), Tohoku University

Address:
Aoba 468-1, Aramaki, Aoba-ku, Sendai 980-8579, Japan

Brief Career:
2010-2012 Assistant Professor, National University of Engineering, Peru
2012-2013 Research Student, ReGiD, IRIDeS, Tohoku University, Japan
2013-2016 PhD Civil Engineering, Graduate School of Engineering, Tohoku University, Japan
2016- JSPS Fellow, IRIDeS, Tohoku University, Japan

Selected Publications:
• B. Adriano, S. Hayashi, H. Gokon, E. Mas, and S. Koshimura, "Understanding the Extreme Tsunami Inundation in Onagawa Town by the 2011 Tohoku Earthquake, Its Effects in Urban Structures and Coastal Facilities," Coastal Engineering Journal, JSCE, Vol.58, pp. 1640013, 2016.

Academic Societies & Scientific Organizations:
• Peruvian Engineering College
• Japan Society of Civil Engineers (JSCE)
• Japan Geoscience Union (JpGU)
• American Geoscience Union (AGU)
• Institute of Electrical and Electronics Engineers (IEEE)

Name:
Erick Mas

Affiliation:
Associate Professor, International Research Institute of Disaster Science (IRIDeS), Tohoku University

Address:
Aoba 468-1, Aramaki, Aoba-ku, Sendai 980-8579, Japan

Brief Career:
1999-2004 B.S. Civil Engineering, National University of Engineering, Peru
2006-2009 M.Sc. Disaster Risk Management, National University of Engineering, Peru
2009-2012 PhD Civil Engineering, Tsunami Engineering, Tohoku University, Japan
2012-2016 Assistant Professor, IRIDeS, Tohoku University, Japan
2016- Associate Professor, IRIDeS, Tohoku University, Japan

Selected Publications:
• E. Mas, B. Adriano, S. Koshimura, F. Imamura, H. Kuroiwa, F. Yamazaki, C. Zavala, and M. Estrada, "Identifying Evacuee's Demand of Tsunami Shelters using Agent Based Simulation. Published on Tsunami Events and Lessons Learned," Y. Kontar, V. Santiago-Fandino, T. Takahashi (Eds.), Springer Netherlands, 2014.
• E. Mas, A. Suppasri, F. Imamura, and S. Koshimura, "Agent Based simulation of the 2011 Great East Japan Earthquake Tsunami evacuation. An integrated model of tsunami inundation and evacuation," Journal of Natural Disaster Science, Vol.34, Issue 1, pp. 41-57, 2012.

Academic Societies & Scientific Organizations:
• Peruvian Engineering College (PEC)
• Japan Society of Civil Engineers (JSCE)
• Japan Geoscience Union (JpGU)
• European Geosciences Union (EGU)
• American Geophysical Union (AGU)

Name:
Hideomi Gokon

Affiliation:
Assistant Professor, Institute of Industrial Science, The University of Tokyo

Address:
4-6-1-Be604, Komaba, Meguro-ku, Tokyo 153-8505, Japan

Brief Career:
2012-2015 Doctoral Course Student, Graduate School of Engineering, Tohoku University
2012-2015 JSPS Research Fellow (DC1)
2012 Visiting Researcher of German Aerospace Center (DLR)
2015-present Assistant Professor, ,Institute of Industrial Science, The University of Tokyo

Selected Publications:
• H. Gokon, J. Post, E. Stein, S. Martinis, A. Twele, M. Muck, C. Gei, S. Koshimura, and M. Matsuoka, "A method for detecting devastated buildings by the 2011 Tohoku Earthquake tsunami using multi-temporal TerraSAR-X data," IEEE Geo- science and Remote Sensing letters, No.6, pp. 1277-1281, 2015.
• H. Gokon, S. Koshimura, K. Imai, M. Matsuoka, Y. Namegaya, and Y. Nishimura, "Developing fragility functions for the areas affected by the 2009 Samoa earthquake and tsunami," Nat. Hazards Earth Syst. Sci., Vol.14, pp. 3231-3241, 2014.

Academic Societies & Scientific Organizations:
• Japan Society of Civil Engineers (JSCE)

Name:
Shunichi Koshimura

Affiliation:
Professor, Laboratory of Remote Sensing and Geoinformatics for Disaster Management, International Research Institute of Disaster Science, Tohoku University

Address:
Aoba 6-6-03, Sendai 980-8579, Japan

Brief Career:
2002-2005 Research Scientist, Disaster Reduction and Human Renovation Institute, Japan
2005-2012 Associate Professor, Tohoku University, Japan
2012- Professor, ReGiD, IRIDeS, Tohoku University, Japan

Selected Publications:
• S. Koshimura, T. Oie, H. Yanagisawa, and F. Imamura, "Developing fragility functions for tsunami damage estimation using numerical model and post-tsunami data from Banda Aceh, Indonesia," Coastal Engineering Journal, No.3, pp. 243-273, 2009.
• S. Koshimura, Y. Hayashi, K. Munemoto, and F. Imamura, "Effect of the Emperor seamounts on trans-oceanic propagation of the 2006 Kuril Island earthquake tsunami," Geophysical Research letters, Vol.35, L02611, doi:10.1029/2007GL032129, 24, 2008.
• S. Koshimura, T. Katada, H. O. Mofjeld, and Y. Kawata, "A method for estimating casualties due to the tsunami inundation flow," Natural Hazards, Vol.39, pp. 265-274, 2006.

Academic Societies & Scientific Organizations:
• Japan Society of Civil Engineers (JSCE)
• Institute of Social Safety Science (ISSS)
• Japan Associaiton for Earthquake Engineering (JAEE)
• Japan Society for Computational Engineering and Science (JSCES)
• Americal Geophysical Union (AGU)